Decadal Variability of Two Oceans and an Atmosphere

BLANCA GALLEGO

Department of Atmospheric Sciences, University of California, Los Angeles, Los Angeles, California

PAOLA CESSI

Scripps Institution of Oceanography, University of California, San Diego, La Jolla, California

(Manuscript received 5 May 2000, in final form 25 October 2000)

ABSTRACT

A model of the midlatitude, large-scale interaction between the upper ocean and the troposphere is used to illustrate possible mechanisms of connection between the decadal variability in the North Atlantic and in the North Pacific. The two ocean basins are connected to each other only through their coupling to the common, zonally averaged atmosphere. The ocean–atmosphere coupling takes place via wind-driven torques and heat fluxes at the air–sea interface. In this formulation, the decadal variability in each ocean basin consists of ocean–atmosphere modes and arises from a delayed feedback of the upper-ocean heat content onto the wind-driven flow mediated by the atmosphere through the requirements of global heat and momentum balances. The presence of two ocean basins leads to three basic kinds of coupling-induced behavior: phase locking, oscillation death, and chaos. In the phase-locked regime, the western boundary currents of the two basins oscillate in synchrony, with the narrower basin following the wider basin by a small time lag. In the oscillation death solutions, a steady solution is reached, even though each ocean basin, when uncoupled, would have sustained oscillations. In the chaotic regime, the interbasin coupling induces aperiodic fluctuations in both basins characterized by variability at centennial, as well as decadal, timescales.

1. Introduction

There is observational evidence of large-scale oceanic and atmospheric decadal variability in both the North Atlantic and the North Pacific basins. This variability is characterized by coherent, basin-scale spatial patterns of oceanic sea surface temperature (SST) anomalies that are correlated to anomalies of atmospheric sea level pressure (SLP; e.g., Deser and Blackmon 1993; Graham 1994; Kushnir 1994; Trenberth and Hurrell 1994; Latif and Barnett 1994, 1996; Nakamura et al. 1997). In the atmosphere, the variability is associated with changes in the surface westerlies and in the patterns of precipitation and surface air temperature over the ocean basins and adjacent land areas (Wallace and Gutzler 1981; Moses et al. 1987; Parker and Folland 1988; Kushnir and Wallace 1989; Trenberth and Hurrell 1994; Hurrel 1995). In the ocean, the variability results in fluctuations of the subsurface ocean temperature and of the oceanic mass transport (Levitus et al. 1994; Deser et al. 1996; McCartney et al. 1997; Zhang and Levitus 1997; Curry et al. 1998).

Corresponding author address: Dr. Paola Cessi, UCSD-0230, Scripps Institution of Oceanography, University of California, San Diego, La Jolla, CA 92093-0230.
E-mail: pcessi@ucsd.edu

An increasing number of climate models have been used to understand the nature and causes of the midlatitude variability at interannual and interdecadal timescales. These studies span a wide spectrum of complexity, ranging from simple analytical formulations of ocean–atmosphere modes to the more complex coupled ocean–atmosphere general circulation models (GCMs). As a result, several mechanisms for low-frequency variability at midlatitudes have been invoked:

- The low-frequency variability is a result of the internal dynamics of the atmosphere. The role of the ocean is to selectively enhance the natural low-frequency variability in the midlatitude atmosphere through reduced thermal coupling (Battisti et al. 1995; Delworth 1996; Bladè 1997; Saravanan 1998).
- The low-frequency variability is a result of the internal dynamics of the ocean, which can force long-term fluctuations in the atmosphere. Self-sustained decadal oceanic modes of variability have been found in both the thermohaline circulation (Weaver et al. 1991; Weaver and Sarachik 1991; Delworth et al. 1993; Winton and Sarachik 1993; Chen and Ghil 1995) and the wind-driven circulation (Speich et al. 1995; Spall 1996; Berloff and Meacham 1997). Weakly damped internal oceanic modes can be excited by stochastic atmospheric forcing (Griffies and Tziperman 1995;

Frankignoul et al. 1997; Saravanan and McWilliams 1997; Saravanan et al. 2000).

- The low-frequency variability is the result of inherently coupled ocean–atmosphere fluctuations. The possibility of coherent, large-scale ocean–atmosphere interaction at midlatitudes was originally hypothesized by Namias (1959) and Namias (1963) in the North Pacific and Bjerknes (1964) in the North Atlantic. Unstable coupled modes with decadal timescales have been found in several modeling studies of the ocean–atmosphere system (Latif and Barnett 1994, 1996; Jin 1997; Grötzner et al. 1998; Munich et al. 1998; Timmermann et al. 1998; Goodman and Marshall 1999; Weng and Neelin 1999; Cessi 2000; Gallego and Cessi 2000).

It is likely that several mechanisms play a role in the low-frequency variability at midlatitudes. For example, Kushnir (1994) suggests that there are two kinds of SST variability in the North Atlantic: an interannual variability forced by the atmosphere and a decadal to interdecadal variability associated with ocean–atmosphere interactions. Also, Barnett et al. (1999) find two kinds of midlatitude Pacific decadal variability in multiple climate simulations: a basinwide variability stochastically forced by the atmosphere with no preferred period, and an oscillatory coupled ocean–atmosphere mode with a period of about 20 years.

Several modeling studies of the decadal variability in the North Atlantic also suggest a significant remote response of the atmosphere over the North Atlantic to climate anomalies in the Pacific region. Atmospheric GCMs forced by observed SSTs show that the decadal variability in SLP over the North Atlantic is associated not only with the SST anomalies in the North Atlantic, but also with those in the Pacific (Latif et al. 2000; Venzke et al. 1999). Decadal modes in the North Atlantic that are linked to the decadal variability in the Pacific sector (Zorita and Frankignoul 1997; Grötzner et al. 1998; Selten et al. 1999) are found in coupled GCMs. Both the degree and the ways in which the variability in the Pacific Ocean influences the variability in the North Atlantic remain to be explained.

Recent analyses of observations also suggest a connection between the decadal variability in the North Atlantic and that in the North Pacific, via the atmosphere. Meehl et al. (1998) found global-scale decadal variability encompassing the Pacific, Atlantic, and Indian Ocean regions. Their analysis of observations and model results show decadal peaks in globally averaged SSTs that occur together with periodic arrangements of the SST anomalies embedded in the various ocean gyre circulations. In-phase decadal oscillations of North Atlantic and North Pacific upper-ocean temperatures are also reported by White and Cayan (1998). Finally, Thompson and Wallace (2000) have suggested that the main mode of variability in the Northern Hemisphere's atmosphere has a spatial structure that is almost zonally symmetric with covarying weak maxima centered over the North Atlantic and the North Pacific basins.

In Gallego and Cessi (2000, hereinafter GC00), we formulated a minimal model of the large-scale interaction between the troposphere and the upper midlatitude ocean. In that formulation, an ocean basin and a zonally averaged atmosphere are coupled through wind stress and heat fluxes at the air–sea interface. Simplified parameterizations, built upon the conservation of global heat and momentum, relate the heat and momentum eddy fluxes in the atmosphere to the zonally averaged oceanic and atmospheric temperatures. The model illustrates, within the framework of large-scale dynamics, how heat and momentum are transported and exchanged in the midlatitude ocean–atmosphere system. The decadal variability thus obtained consists of coupled ocean–atmosphere modes. It arises from a delayed negative feedback between the upper ocean and the atmospheric circulations. In particular, there is a feedback of the upper-ocean heat content onto the wind-driven flow mediated by the atmosphere through the requirements of global heat and momentum balances. Although this feedback is negative, the delayed response of the oceanic circulation to changes in the wind stress can reverse the sign of the feedback leading to sustained oscillations. The period of the oscillations is dictated by the transit time of long Rossby waves across the ocean basin and is of the order of decades.

In the sequel, we examine the large-scale interaction between a zonally averaged atmosphere and the wind-driven oceanic circulation in the Northern Hemisphere by extending the formulation in GC00 to the case in which two ocean basins, the North Atlantic and the North Pacific, are present. The ocean basins are connected to each other through their coupling to the common zonally averaged atmosphere. Thus we take the point of view that the midlatitude atmospheric variability on decadal timescales is dominated by a zonally symmetric (or ''annular'') pattern. Moreover, we focus on changes in the atmospheric eddy flux of momentum and the associated changes in surface wind stress. This approach is consistent with the analysis of Thompson and Wallace (2000), which shows that the annular variability of the Northern Hemisphere is characterized by modulations of the zonally averaged surface winds.

2. The model

Geometry and formulation

The model's geometry is depicted in Fig. 1. The atmosphere occupies a rectangular reentrant channel with zonal and meridional extents given by L_x and L_y, respectively. Each ocean basin covers a fraction r_i (i = 1, 2) of the domain's width so that the oceans' zonal extents are $L_{xi} = r_i L_x$. The oceans' meridional extent is the same as the atmosphere's, L_y, and their mean thermocline depths are denoted by H_i.

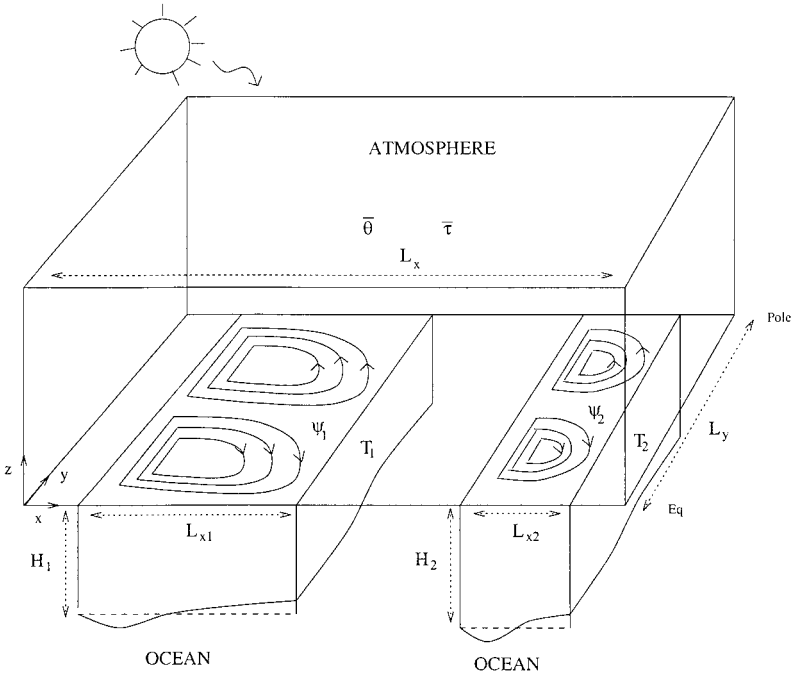

FIG. 1. Schematic picture of the model's geometry.

The ocean basins are connected to each other only through their coupling to the common zonally averaged atmosphere, which takes place via wind-driven torques and heat fluxes at the air–sea interface.

The model equations are the momentum and heat balances in the troposphere and upper oceans. The only forcing of the system is the prescribed incoming net shortwave radiation.

1) THE ATMOSPHERIC MOMENTUM AND HEAT BALANCES

The atmosphere is zonally averaged and in instantaneous equilibrium with the oceans, even if the latter changes with time. The atmosphere is characterized by two diagnostic variables: the zonally averaged surface potential temperature, $\overline{\theta}(y, t)$ and the zonally averaged wind stress, $\overline{\tau}(y, t)$.

Potential temperature $\overline{\theta}$ is determined by the vertically and zonally integrated atmospheric heat budget:

$$C_{pa}\int_0^\infty \rho_a \frac{\partial(\overline{\theta' v'})}{\partial y}\,dz = F_0 + Ff(y) - A - B\overline{\theta} - r_1\lambda(\overline{\theta} - \overline{T}_{S1}) - r_2\lambda(\overline{\theta} - \overline{T}_{S2}). \quad (1)$$

Here, $F_0 + Ff(y)$ is the prescribed incoming net shortwave radiation, with the simple form $f(y) = \cos(\pi y/L_y)$. The outgoing longwave radiation, $A + B\overline{\theta}$, derives from the linearization of the graybody Stefan–Boltzmann law. The last two terms on the right-hand side of (1) are the air–sea heat flux exchanges with the two ocean basins and are proportional to the difference between $\overline{\theta}$ and the zonally averaged sea surface temperatures, $\overline{T}_{S1}$ and $\overline{T}_{S2}$, weighted by the fraction of latitude circles occupied by each basin, r_i. The bulk heat transfer coefficient λ is assumed constant. The left-hand side is the divergence of the zonally averaged heat transport due to atmospheric motion, which is parameterized using (4). Here C_{pa} is the specific heat of the atmosphere and ρ_a is the atmospheric density with the vertical profile $\rho_a = \rho_o \exp(-z/D)$.

The zonally averaged wind stress $\overline{\tau}$ is given by the divergence of the eddy momentum flux:

$$\overline{\tau} = -\int_0^\infty \rho_a \frac{\partial(\overline{u' v'})}{\partial y}\,dz. \quad (2)$$

This relation represents the zonally and vertically averaged momentum budget for the atmosphere in steady state, and in the limit of no mountain torque (Lorenz 1967, p. 51).

In order to relate the eddy flux of momentum to zonally averaged quantities, following Green (1970), we use the quasigeostrophic relation between the zonally averaged eddy fluxes of momentum, heat, and potential vorticity:

$$(\overline{q' v'}) = \frac{f_o}{\rho_a}\frac{\partial}{\partial z}\left[\frac{\rho_a}{S}(\overline{\theta' v'})\right] - \frac{\partial(\overline{u' v'})}{\partial y}. \quad (3)$$

Here S is the atmosphere static stability, f_o is the reference Coriolis parameter, and q denotes potential vorticity. The right-hand side of (3) is the divergence of the Eliassen–Palm flux vector, and this equality allows to relate the wind stress $\overline{\tau}$ to $\overline{\theta}$ and $\overline{q}$. In the spirit of

Green (1970) we then assume that the role of the eddies is to redistribute heat and potential vorticity in such a way as to reduce the large-scale gradients of these two scalar quantities. Furthermore, we choose to parameterize the divergence of the eddy fluxes of heat and potential vorticity as relaxation to their planetary averages, $\overline{\theta}_A$ and $\overline{q}_A$, respectively, rather than as downgradient diffusion, that is:

$$\frac{\partial(\overline{\theta' v'})}{\partial y} = \nu(\overline{\theta} - \overline{\theta}_A), \tag{4}$$

$$\frac{\partial(\overline{q' v'})}{\partial y} = \nu(\overline{q} - \overline{q}_A). \tag{5}$$

The parameterization of eddy heat fluxes in (4) has been used in early energy balance models (Budyko 1969). Here we use the same simplified parameterization for the potential vorticity heat fluxes. This choice adopts the same strategy as Green (1970) and Pavan and Held (1996) of parameterizing the eddy fluxes of heat and potential vorticity in the same fashion.

The eddy relaxation rate ν is of the form, $\nu = \nu_o \exp(-z/d)$, with ν^{-1} on the order of 20 days. The planetary-averaged temperature is determined solely by radiation processes so that

$$\overline{\theta}_A = L_y^{-1} \int_0^{L_y} [F_0 + Ff(y) - A]/B \, dy. \tag{6}$$

The zonally averaged potential vorticity $\overline{q}$ can be accurately approximated with its large-scale limit (Sun and Lindzen 1994), which in the β-plane description is given by

$$\overline{q} = \beta y + \frac{f_o}{\rho_a} \frac{\partial}{\partial z}\left(\frac{\rho_a}{S}\overline{\theta}\right),$$

$$\overline{q}_A = \beta \frac{L_y}{2} + \frac{f_o}{\rho_a} \frac{\partial}{\partial z}\left(\frac{\rho_a}{S}\overline{\theta}_A\right). \tag{7}$$

Assuming that $\overline{\theta}$ and S are independent of z, as in a two-level model, $\overline{\tau}$ is then entirely determined by $\overline{\theta}$ through the relation:

$$\frac{\partial \overline{\tau}}{\partial y} = d_e \rho_o \nu_o \left[\beta\left(y - \frac{L_y}{2}\right) + \frac{f_o}{Sd}(\overline{\theta} - \overline{\theta}_A)\right]. \tag{8}$$

The parameter d_e has been defined as the effective eddy-scale height given by $d_e^{-1} = D^{-1} + d^{-1}$, where the density-scale height D is prescribed and the eddy-scale height d is determined by enforcing the condition of no net surface torque. The relation (8) clearly shows that the wind stress curl decreases with reduced north–south temperature differences.

Using (4) in the energy balance (1), $\overline{\theta}$ is determined by the sea surface temperatures $\overline{T}_{S1}$ and $\overline{T}_{S2}$ and the incoming radiation through the relation:

$$\overline{\theta} - \overline{\theta}_A = \frac{[r_1\lambda(\overline{T}_{S1} - \overline{\theta}_A) + r_2\lambda(\overline{T}_{S2} - \overline{\theta}_A) + Ff(y)]}{[C_{pa}\rho_o\nu_o d_e + B + (r_1 + r_2)\lambda]}. \tag{9}$$

Thus the atmospheric variables are determined once the oceanic surface temperatures T_{Si} are known.

2) The oceanic momentum and heat balances

In each ocean basin, we identify the sea surface temperature T_{Si} with the oceanic temperature vertically averaged over the depth of the ocean above the thermocline located at $z = -H_i$. The evolution of the vertically averaged upper-ocean temperatures T_{S1} and T_{S2} is described by the heat budgets:

$$C_{pw}\rho_w H_i\left[\frac{\partial T_{Si}}{\partial t} + J(\psi_i, T_{Si}) - \epsilon\nabla^2 T_{Si}\right] = \lambda(\overline{\theta} - T_{Si}), \qquad (i = 1, 2). \tag{10}$$

Variables C_{pw} and ρ_w are the specific heat and density of seawater and ϵ is the eddy diffusivity due to small-scale oceanic motions. Here ψ_1 and ψ_2 are the streamfunctions of the oceanic flows averaged over the depth of the thermocline. Thus we treat the upper-ocean temperature as a passive tracer advected by the oceanic flows and forced by the air–sea heat fluxes. The oceanic currents are determined by the wind stress through the time-dependent Sverdrup balance:

$$\frac{\partial \psi_i}{\partial t} - c_i\frac{\partial \psi_i}{\partial x} = \frac{R_i^2}{\rho_w H_i}\frac{\partial \overline{\tau}}{\partial y} + c_i\delta_i\nabla^2\psi_i, \qquad (i = 1, 2). \tag{11}$$

Here R_i are the baroclinic deformation radii, assumed to be constant; $c_i = \beta R_i^2$ are the speeds of the long Rossby waves, and δ_i are the widths of the western boundary layers. Equation (11) is the reduced-gravity potential vorticity equation in the limit where the scale of the motion is much larger than R_i and it approximately describes the linear evolution of the upper-ocean currents, assuming that the water below $z = -H_i$ is at rest, and in the context of the quasigeostrophic β-plane approximation (cf. Salmon 1998, chapter 3.12). In the limit $\delta_i \ll L_{xi}$, the solutions of (11) have the form:

$$\psi_i = \psi_{Ii}(x, y, t) - \psi_{Ii}(0, y, t)\exp(-x/\delta_i) + O(\delta_i/L_{xi}), \tag{12}$$

which satisfy the condition of no normal flow, $\psi_i = 0$, at $x = 0, L_{xi}$. Here ψ_{Ii} are the interior streamfunctions, determined by the wind stress curl through the time-dependent Sverdrup relation (Anderson and Gill 1975):

$$\psi_{Ii}(x, y, t) = \frac{R_i^2}{\rho_w H_i}\int_{t-(L_{xi}-x)/c_i}^{t} \frac{\partial \overline{\tau}(y, t')}{\partial y}\, dt'. \tag{13}$$

3) SIMPLIFICATION IN THE RAPID RELAXATION LIMIT

In the limit where the timescale of the local air–sea heat exchange, $C_{pw}\rho_w H_i \lambda^{-1}$, is much shorter than the timescale of oceanic advection, it is possible to obtain a relation between the zonally averaged poleward heat transport and the zonally averaged oceanic temperature (GC00; Wang et al. 1995). This limit reduces the two-dimensional evolution of the ocean temperatures (10) to one-dimensional equations for the zonally averaged components. In this approximation, the role of the meridional heat transport by the gyres is to redistribute heat down the mean oceanic temperature gradient with a ''diffusivity'' proportional to the square of the oceanic velocity,

$$\overline{v_i T_{Si}} \approx -\lambda^{-1} C_{pw}\rho_w H_i \overline{v_i^2} \frac{\partial \overline{T}_{Si}}{\partial y}, \tag{14}$$

where $v_i = \partial_x \psi_i$.

A zonally averaged meridional transport of heat is obtained only if the oceanic temperature varies with longitude. Otherwise, a gyre would transport water northward at the same temperature as that carried southward, with no net heat transport. With an atmospheric forcing that is constant in x, longitudinal variations in oceanic temperature can only arise because the gyral circulation turns *meridional* temperature gradients into *zonal* temperature gradients. Hence the *quadratic* dependence of the heat transport on the velocity in (14). Furthermore, $\overline{v_i^2}$ is dominated by the western boundary current contribution and to leading order in δ_i/L_{xi}, it is given by

$$\overline{v_i^2} \simeq \frac{\psi_{Wi}^2}{2\delta_i L_{xi}}, \tag{15}$$

where $\psi_{Wi} \equiv \psi_{Ii}(0, y, t)$ are the interior streamfunctions evaluated at the western boundaries of each ocean basin and ψ_{Ii} is given in (13). Here $H_i\psi_{Wi}$ measures the maximum transport of the western boundary current.

In this way, the two-dimensional oceanic heat and momentum balances (10) and (11), can be reduced to one-dimensional evolution equations for the zonally averaged basin temperatures $\overline{T}_{Si}$. The western boundary transport per unit depth, ψ_{Wi}, can be determined using (13), evaluated at $x = 0$. Then, using the diagnostic expressions for $\overline{\tau}_y$ and $\overline{\theta}$, (8) and (9) respectively, the final set of the model equations is given by

$$\psi_{Wi} = \frac{R_i^2}{\rho_w H_i} \int_{t-t_{oi}}^{t} d_e \rho_o \nu_o \left\{ \beta\left(y - \frac{L_y}{2}\right) + \frac{f_o \Gamma}{Sd}[r_1 \lambda \overline{T}_1 + r_2 \lambda \overline{T}_2 + Ff(y)] \right\} dt', \tag{16}$$

$$\frac{\partial \overline{T}_i}{\partial t} = \Upsilon_i \frac{\partial}{\partial y}\left(\psi_{Wi}^2 \frac{\partial \overline{T}_i}{\partial y}\right) - \frac{\lambda \Gamma}{C_{pw}\rho_w H_i}[\Lambda \overline{T}_i + \lambda r_j(\overline{T}_i - \overline{T}_j) - Ff(y)] + \epsilon \frac{\partial^2 \overline{T}_i}{\partial y^2}, \tag{17}$$

where $\Upsilon_i \equiv C_{pw}\rho_w H_i/(2\lambda\delta_i L_{xi})$, $\Gamma \equiv [C_{pa}\rho_o \nu_o d_e + B + (r_1 + r_2)\lambda]^{-1}$ and $\Lambda \equiv C_{pa}\rho_o \nu_o d_e + B$. The subscripts $(i, j) = (1, 2)$ or $(2, 1)$ refer to the two ocean basins; $\overline{T}_i$ represent the departure of the zonally averaged basin temperatures from the planetary average, $\overline{T}_i \equiv \overline{T}_{Si} - \overline{\theta}_A$. The boundary conditions are no normal heat flux, $\partial_y \overline{T}_i = 0$ at $y = 0, L_y$. We have also defined the delay times $t_{oi} = L_{xi}/c_i$: these are the times taken by long baroclinic Rossby waves to make one east–west transit across each ocean basin.

Equation (16) describes the baroclinic response of the oceans to the wind stress in turn due to changes in the oceanic surface temperature distribution. In this sense, the oceanic temperature is not passively advected by the oceanic flow: its distribution affects the oceanic currents by affecting the wind stress curl through the atmospheric temperature. The zonally averaged atmospheric temperature is determined by a linear combination of the zonally averaged temperatures in the ocean basins, $r_1\overline{T}_1 + r_2\overline{T}_2$. As a result, in each basin, the oceanic interior transport, $\psi_{Wi}(y, t)$, is given by the time histories of $\overline{T}_1$ and $\overline{T}_2$ from the delayed time $t - t_{oi}$ to the actual time t.

Equation (17) describes the evolution of the zonally averaged ocean temperatures due to meridional advection by the gyres, relaxation to the atmospheric temperature through surface heat fluxes, and diffusion by small-scale motions. In this formulation, the role of the meridional heat transport by the gyres [the first term on the right-hand side of (17)] is to redistribute heat down the mean gradient, with a diffusivity proportional to the square of the oceanic velocity at the seaward edge of the western boundary current.

The model Eqs. (16) and (17) follow naturally from the model equations for the single basin case; the reader interested in a detailed derivation is referred to GC00.

4) INTERBASIN COUPLINGS

There are two ways in which the ocean–atmosphere coupling takes place and, therefore, two ways in which the two ocean basins interact with each other.

There is a delayed interbasin coupling that takes place through the oceanic northward heat transport, proportional to $-\psi_{Wi}^2 \partial_y \overline{T}_i$ in (17). In each basin, the ocean circulation ψ_{Wi} is determined by the time history of both $\overline{T}_1$ and $\overline{T}_2$ all the way back to the delayed times $t - t_{oi}$, through the terms proportional to $r_1\overline{T}_1 + r_2\overline{T}_2$ in (16). Thus, the divergence of oceanic heat transport, in the form of a nonlinear diffusion term, represents a negative delayed feedback.

The second term on the right-hand side of (17) is proportional to the divergence of the atmospheric heat transport, and is in the form of a (undelayed) negative feedback. This term contains an instantaneous interbasin coupling that takes place through the relaxation of the ocean temperatures to the common atmospheric temperature $\overline{\theta}$ which in turn depends on both $\overline{T}_1$ and $\overline{T}_2$ [proportional to $r_j(\overline{T}_i - \overline{T}_j)$ in (17)]. It restores the oceanic temperatures towards a common equilibrium temperature determined by air–sea heat fluxes. In the absence of ocean circulation, this instantaneous coupling would lead the system to a steady state where $\overline{T}_1 = \overline{T}_2 = Ff(y)/\Lambda$.

3. Coupling-induced phenomenology

It was shown in GC00 that when only one basin is present, there is a region in the parameter space in which the system settles into periodic solutions. These sustained oscillations are coupled ocean–atmosphere modes characterized by large-scale temperature anomalies of small amplitude and decadal period. Although the gyres transport heat downgradient, so that the wind-driven circulation reduces the wind stress curl and the thermal feedback of the ocean flow on the wind stress is negative, because the response of the ocean to changes in the wind stress is delayed, growth of oceanic temperature anomalies occurs for part of the cycle. Thus, the solutions can be oscillatory with a period that is about twice the transit time of long Rossby waves across the ocean basin.

The system of a single ocean basin and the atmosphere is a nonlinear oscillator with a rich dynamics: phase-space trajectories can approach asymptotically either a chaotic or a nonchaotic attractor. That is, fixed points, periodic limit cycles, quasiperiodic attractors, and more complicated chaotic structures can be visited as the control parameters are varied. In GC00, we discussed only the transition from fixed points to limit cycles. In the sequel, we document the basic coupled-induced phenomena generic to nonlinear coupled oscillators: 1) a phase-locked solution in which the two oscillators share a common frequency, 2) an ''oscillation death'' solution in which the system goes to a fixed point far from the limit cycles of the individual oscillators, and 3) an aperiodic solution in which the system exhibits chaotic behavior with the oscillators varying aperiodically in time.

a. Phase locking

In this section we present the results obtained by solving (16) and (17) numerically. At each time step t_n, the knowledge of the temperature fields at times $t_n - t_{oi}$ is required. The radiative equilibrium temperature is used as the initial condition for both basins and the temperature fields before $t = 0$ are assumed to be constant in time and equal to the initial condition.

Table 1 lists parameter values that are appropriate for the midlatitude Northern Hemisphere troposphere and the midlatitude North Pacific and North Atlantic upper oceans. Subscripts 1 and 2 refer to the Pacific and to the Atlantic basins, respectively. Some of these values are poorly constrained by observations. For example, the relaxation time toward the planetary averaged temperature (and potential vorticity), ν_0^{-1}, is taken to be 23 days, a typical value used in energy balance models (Budyko 1969). The value for the air–sea heat exchange is here taken to be $\lambda = 30$ W m^{-2} °C^{-1}, i.e., at the low end of the range quoted by Haney (1971). Fortunately, the qualitative behavior of our model does not depend sensitively on these choices, although the quantitative results do. For the values listed in Table 1, the solution to (16) and (17) has sustained oscillations where the physical fields of the two basins fluctuate at a common frequency with a period of about 38 yr.

Figure 2 shows some of the time-averaged fields as a function of latitude. The time- and zonally averaged ocean temperatures are very similar in both basins and closely follow the time- and zonally averaged atmospheric potential temperature at the surface. The maximum difference between atmospheric and oceanic temperatures is about 1°C and occurs at the center of the gyres. As expected from Sverdrup balance, the strength of the flow at the western boundary is larger in the Pacific, ψ_{W1}, than in the Atlantic, ψ_{W2}, by a factor of $H_1L_{x1}/(H_2L_{x2})$. This leads to a zonally averaged northward oceanic heat transport in the Pacific that is about twice that in the Atlantic. The oceanic heat transport in each basin is given by an advective part, which peaks at the maximum of the gyres' transport, and a diffusive part, which is responsible for the heat transport at the intergyre boundary and is subdominant elsewhere.

The zonally averaged wind stress can be diagnosed by integrating (8) in latitude and assuming that $\overline{\tau}$ vanishes at $y = 0$. The wind stress thus obtained is smaller than that observed, even though the atmospheric heat transport (AHF) has values close to the observations. This discrepancy is due to the highly idealized shape of the radiative forcing and can be remedied with more realistic choices [e.g., that used in Cessi (2000)]. However, we prefer to retain an idealized symmetric shape of the forcing, at the cost of a loss in realism, because this allows us to capture the spontaneous symmetry breaking of the system. Naturally, the small values of wind stress lead to interior oceanic circulations weaker than those observed. Nevertheless, the zonally averaged

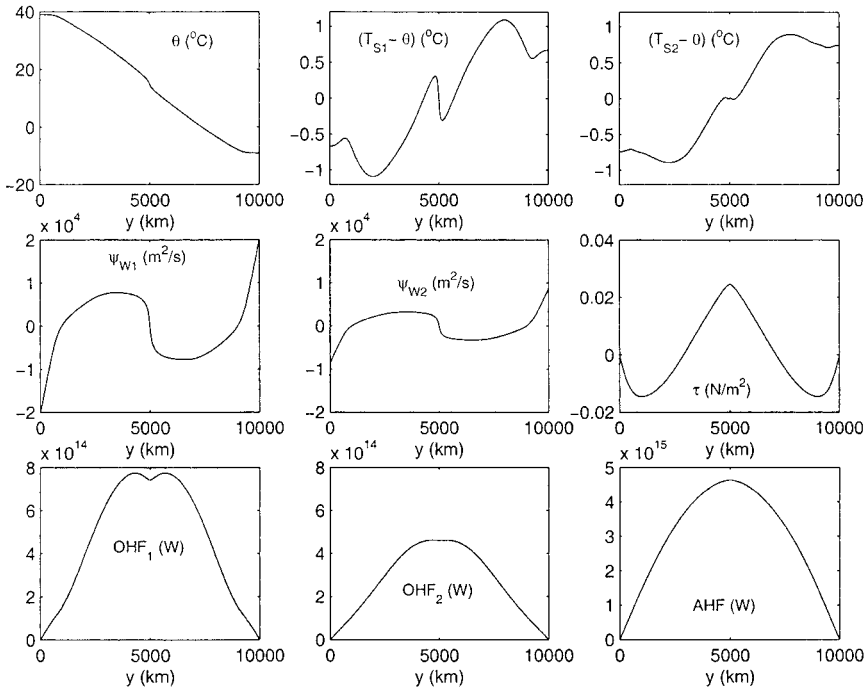

FIG. 2. Various time-averaged fields as a function of latitude. (top row) Zonally averaged atmospheric surface potential temperature $\overline{\theta}$ and departures from $\overline{\theta}$ of the zonally averaged oceanic temperature in the Pacific ($\overline{T}_{S1} - \overline{\theta}$) and in the Atlantic ($\overline{T}_{S2} - \overline{\theta}$). (middle row) Western boundary interior streamfunctions ψ_{w1} and ψ_{w2} and zonally averaged atmospheric wind stress $\overline{\tau}$. (bottom row) Zonally averaged northward heat transport in the ocean basins, OHF_1 and OHF_2, and in the atmosphere, AHF. The planetary averaged temperature and $\overline{\theta}_A$ is set at 15°C.

Pacific poleward heat transport (OHF_1) peaks at a value that is consistent with the current estimates. Because in the rapid relaxation limit the heat transport is dominated by the western boundary contribution, a narrow boundary layer width compensates for the weakness of the interior transport. The Atlantic northward heat transport (OHF_2) is smaller than the observed estimate, as expected in the absence of a thermohaline circulation.

As in GC00, the time-periodic ocean temperature and transport anomalies[1] (not shown here) are antisymmetric about the central latitude of the domain and occupy the entire latitudinal extent of the gyres.

Figure 3 shows the evolution in time for the same run of the heat transport anomalies in the atmosphere and in each ocean basin. The atmospheric heat transport (right panel) oscillates approximately out of phase with respect to the oceanic ones and the wider basin (left panel) leads the narrow one (middle panel) by a few years. The approximate quadrature of the fluctuations between the atmospheric and the oceanic heat transports is the hallmark of a coupled mode of variability where the OHF is a delayed negative feedback and the AHF is an instantaneous negative feedback.

The common period at which the phase-locked solution oscillates is dictated by the delay times in the ocean basins, t_{o1} and t_{o2}. Figure 4 shows contour plots of the period as a function of the delay times, obtained by varying R_1 and R_2 from 22 to 30 km. The period is close to that obtained with the Pacific only, as expected from the fact that the Pacific basin is wider. Specifically, the dominant period is that of the oscillator with the largest amplitude when uncoupled. Additional analysis, not presented here, shows that the oscillation's amplitude for an uncoupled basin increases with the basin width. Thus, because the Atlantic basin is narrower, it has, when uncoupled, a weaker influence on the atmosphere and thus admits oscillations of small amplitude or damped, while the wider Pacific basin exhibits sustained periodic solutions of larger amplitude. Thus the period of the Pacific dominates over that of the Atlantic in the phase-locked coupled solution.

b. Oscillation death

When the long Rossby wave delays for the two ocean basins are different enough, the oscillatory anomalies decay in time and the system eventually reaches a steady state, even if each individual basin has sustained oscillations when uncoupled.

The phenomenon of oscillation death has been observed in systems of coupled oscillators when the cou-

[1] Anomalies are defined as departures of the field from the time average.

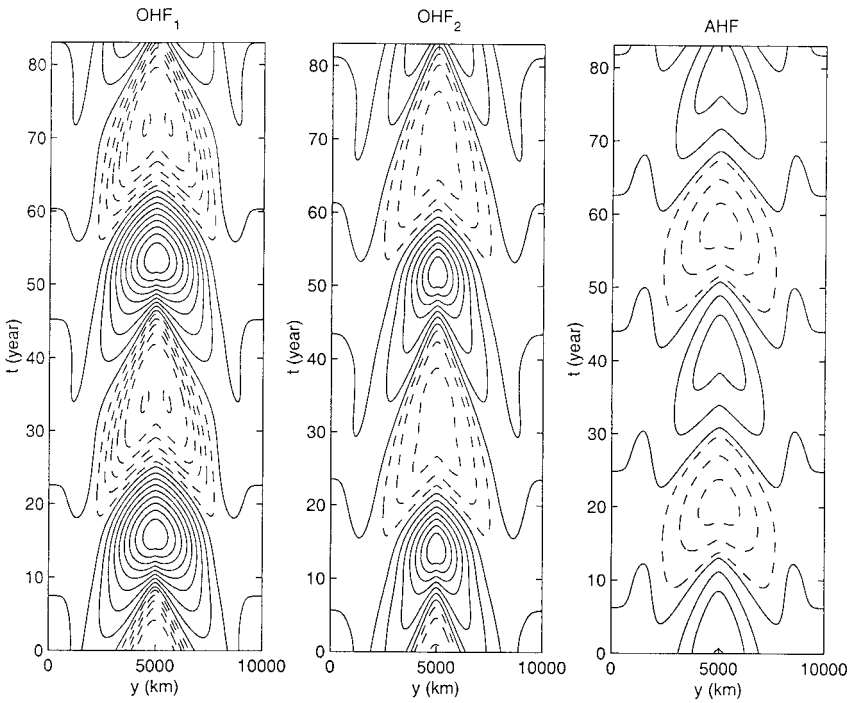

FIG. 3. Anomalies of the zonally averaged northward heat transport in the (left) Pacific basin, in the (middle) Atlantic basin, and in the (right) atmosphere as a function of latitude and time during two periods of the oscillation. Negative values are dashed. The maximum values of the anomalies in the Pacific, the Atlantic, and the atmosphere are 8.8×10^{14} W, 6.9×10^{14} W, and 2.4×10^{14} W, respectively. The contour interval is 1×10^{14} W for all panels.

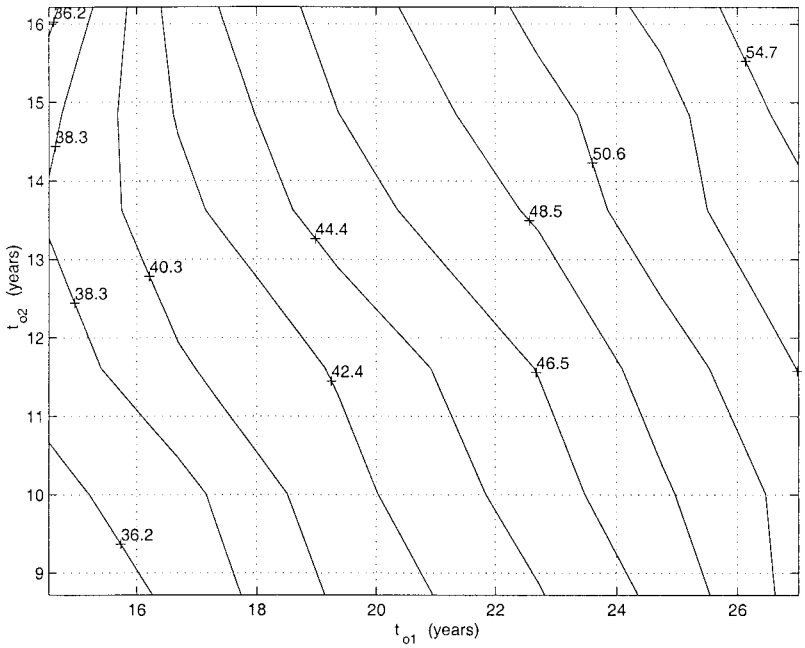

FIG. 4. Contour plot of the period of the oscillations as a function of the Pacific (abscissa) and Atlantic (ordinate) delay times. The contour labels indicate the period in years.

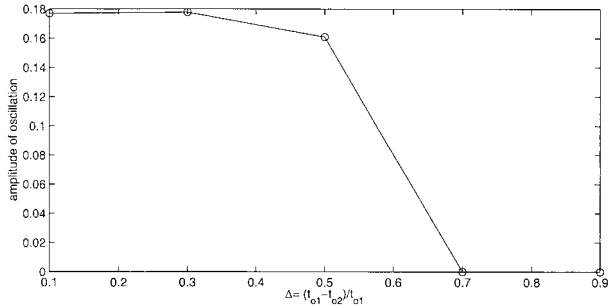

FIG. 5. Transition from phase-locked solutions to oscillation death solutions as the difference between the delay times in the Pacific and in the Atlantic increases. The abscissa is the normalized difference between delayed times, $\Delta = (t_{o1} - t_{o2})/t_{o1}$, and the ordinate is a measure of the amplitude of the oscillation.

pling is sufficiently strong and when the difference between the natural frequencies of the oscillators is above a certain threshold. In this case the oscillators cannot phase lock to a common frequency.

In our formulation, GC00 show that the parameter controlling the natural frequency of oscillation in each basin is the long Rossby wave delay time. Figure 5 illustrates the transition from phase-locked solutions to oscillation death solutions as the delay time in the Pacific, t_{o1}, is increased while keeping the delay time in the Atlantic, t_{o2}, fixed. The horizontal axis is the normalized difference between delay times $\Delta = 1 - t_{o2}/t_{o1}$. The vertical axis is a measure of the amplitude of the oscillation given by

$$\text{amplitude} \equiv \frac{\max_y(\overline{T}_1 - \langle\overline{T}_1\rangle) - \min_y(\overline{T}_1 - \langle\overline{T}_1\rangle)}{\max_y(\langle\overline{T}_1\rangle) - \min_y(\langle\overline{T}_1\rangle)}, \quad (18)$$

where the angle brackets indicate the time average. Variations in t_{o1} are obtained by changing the Rossby deformation radius of the Pacific, R_1, from 34.3 km ($\Delta = 0.1$) to 11.4 km ($\Delta = 0.9$). This range is well within that spanned by the observational estimates of the global zonally averaged first baroclinic radius for the world ocean, which varies from 230 km at the equator to 10 km at the northernmost latitudes (Chelton et al. 1998).

The other parameters are kept constant and equal to those given in Table 1. For $\Delta \geq 0.7$ ($R_1 \leq 20$ km) there are no sustained phase-locked oscillations and the system reaches a steady state.

Figure 6 shows the anomalies in the zonally averaged sea surface temperature, $r_1\overline{T}_1 + r_2\overline{T}_2$, and in the oceanic transports, ψ_{W1} and ψ_{W2}, as a function of time at the latitude $y = 4000$ km, located in the subtropical gyres. The top panel corresponds to the solution described in the previous section where $R_1 = 28$ km and the system settles into a limit cycle. The bottom panel corresponds to a calculation with the same parameter values except that $R_1 = 18$ km, so that oscillation death takes place and the system goes to a fixed point. The anomalies have been normalized by their maximum values.

In the case of sustained, phase-locked oscillations, the fluctuations in sea surface temperature are approximately in quadrature with the fluctuations of the oceanic transport in both basins. Also, ψ_{W1} and ψ_{W2} oscillate with a phase shift of about 5 yr. This phase shift is due to the difference between the delay times of the basins and is much smaller than the period of the oscillations (37 yr). In other words, the response time of the Pacific and Atlantic circulations to changes in the common wind stress curl is longer than the difference in these response times between the two basins. Therefore, the coupled system can find a compromise frequency that preserves the temporal structure of the feedback between the oceanic heat transport anomalies and the atmospheric temperature anomalies, necessary for the oscillations to be sustained. As a result, an anomaly in the surface temperature grows during the time where the ocean circulations are still influenced by the opposite sign anomaly that occurred in the past 5–17 yr. The growing temperature anomaly eventually changes the sign of the ocean circulations; then, the resulting oceanic heat transports begin to reduce the temperature anomaly and eventually reverse the temperature tendency.

However, if the Atlantic Ocean adjusts to changes in the surface temperature much more rapidly than the Pacific Ocean, it can break the temporal structure of the delayed negative feedback mechanism, taking the entire coupled system to a state of rest. This is the case for the oscillation death solution represented in the bottom panel of Fig. 6: the oceanic transport anomalies ψ_{W1} and ψ_{W2} are approximately in quadrature, with ψ_{W2} following closely the variations in surface temperature. Each time an anomaly in $r_1\overline{T}_1 + r_2\overline{T}_2$ grows, the wind stress curl increases, thus spinning up the circulation in the Atlantic with a small delay. This decreases the temperature in

TABLE 1. Parameter values for Figs. 1 and 2. In this case the delays are $t_{o1} = 16.7$ yr and $t_{o2} = 10.0$ yr.

$L_{x1} = 8.25 \times 10^6$ m	$L_y = 1 \times 10^7$ m	$\rho_o = 1.25$ kg m^{-3}	$F_0 - A = 37.5$ W m^{-2}
$L_{x2} = 4.95 \times 10^6$ m	$L_x = 2.75 \times 10^7$ m	$\rho_w = 1000$ kg m^{-3}	$B = 2.5$ W m^{-2} °C^{-1}
$H_1 = 700$ m	$\delta_1 = 5.1 \times 10^4$ m	$C_{pa} = 1000$ J °C^{-1} kg^{-1}	$F = 125$ W m^{-2}
$H_2 = 1000$ m	$\delta_2 = 5.1 \times 10^4$ m	$C_{pw} = 4000$ J °C^{-1} kg^{-1}	$S = 5 \times 10^{-3}$ °C m^{-1}
$R_1 = 2.8 \times 10^4$ m	$D = 10^4$ m	$\nu_o = 5 \times 10^{-7}$ s^{-1}	$f_o = 10^{-4}$ s^{-1}
$R_2 = 2.8 \times 10^4$ m	$\lambda = 30$ W m^{-2} °C^{-1}	$\epsilon = 1.2 \times 10^3$ m^2 s^{-1}	$\beta = 2 \times 10^{-11}$ m^{-1} s^{-1}

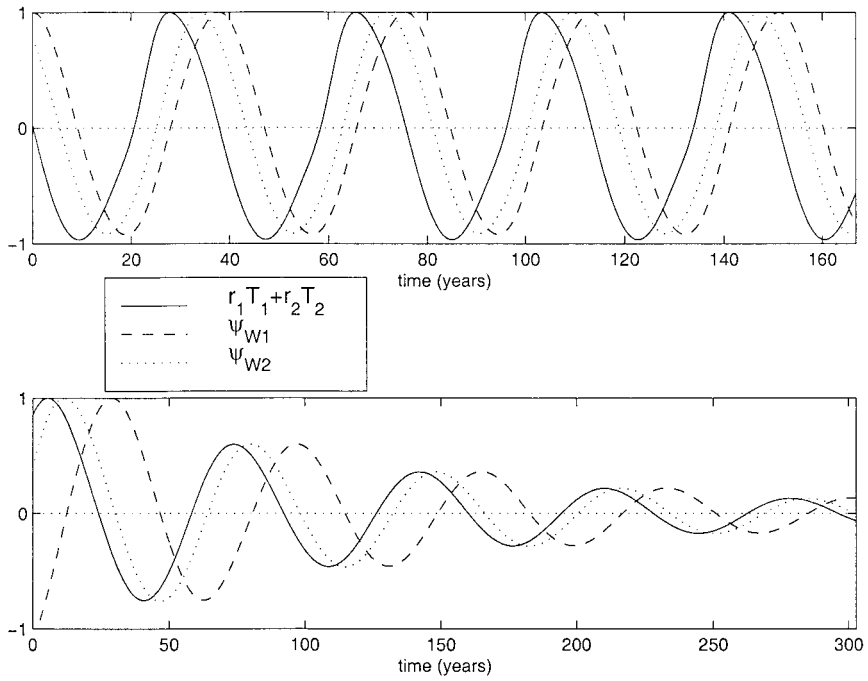

FIG. 6. Anomalies of the zonally averaged sea surface temperature, $r_1\overline{T}_1 + r_2\overline{T}_2$ (solid line) and of the interior oceanic transports at the western edge in the Pacific, ψ_{W1} (dashed line), and in the Atlantic, ψ_{W2} (dotted line), as a function of time at the latitude $y = 4000$ km. Each field has been normalized to its maximum value. (top) The phase-locked solution with parameter values given in Table 1. (bottom) An oscillation death solution with the same parameter values except that $R_1 = 18$ km.

the Atlantic, $\overline{T}_2$, so that the anomaly in the Pacific, $\overline{T}_1$, is relaxed toward a smaller temperature anomaly and thus saturates at a smaller amplitude. Eventually, the system reaches a steady state.

c. Chaos

In the region of parameter space where the amplitude of the decadal variability is large enough, aperiodic behavior is obtained.

Large amplitude anomalies are found if the value of the bulk transfer coefficient is increased to $\lambda = 50$ W m^{-2} °C^{-1} and the width of the western boundary layers is decreased to $\delta_1 = \delta_2 = 5.2$ km. These changes imply a larger heat exchange between the atmosphere and the oceans, as well as larger oceanic northward heat transports. As a result, the delayed feedback mechanism, which is responsible for the generation of the variability, becomes more effective, leading to larger amplitude fluctuations. In this formulation, the appearance of chaos requires unrealistically small values of the western boundary layer widths. However, our linearized ocean dynamics (11) underestimates the transport of the boundary currents because the wind stress curl is too weak and inertial effects are neglected. It is possible that chaos would arise with a western boundary current that is more realistically sized, but is of higher amplitude and inertial.

Using the new values of λ and δ_i we find two regions of chaotic solutions as the difference between delay times, Δ, is varied. The chaotic solutions, which we have called chaos 1 and chaos 2, are separated by a region of phase-locked solutions. As in the previous section, variations in Δ are obtained by changing the Rossby deformation radius of the Pacific basin, R_1. Also here, $H_1 = H_2 = 1$ km and $R_2 = 30$ km. Chaotic solutions of type 1 are obtained for values of $\Delta \leq 0.55$ ($R_1 \geq 26$ km). Chaotic solutions of type 2 occur for values of Δ centered around 0.85 ($R_1 \approx 15$ km). The main difference between the two kinds of chaotic solutions is that in the second kind, the system fluctuates between having most of the variability concentrated in the subtropical gyres to having it concentrated in the subpolar gyres while in the first kind this alternation is not present.

Figures 7 and 8 show analysis of the time series for the solutions corresponding to $R_1 = 30$ km (Fig. 7) within the chaos 1 region, and to $R_1 = 16$ km (Fig. 8) within the chaos 2 region. The panels on the left, show a section of the time series of the Pacific temperature anomalies $\overline{T}_1$ at a given latitude $y = 4000$ km (top), and the corresponding power spectrum (bottom). The top panels on the right show the phase plane of the ocean temperature anomalies at the same latitude, $\overline{T}_1$ versus $\overline{T}_2$. The bottom panels on the right show a Poincarè section of the trajectory crossing the surface $\overline{T}_2 = 0$ while going forward in time from positive to negative

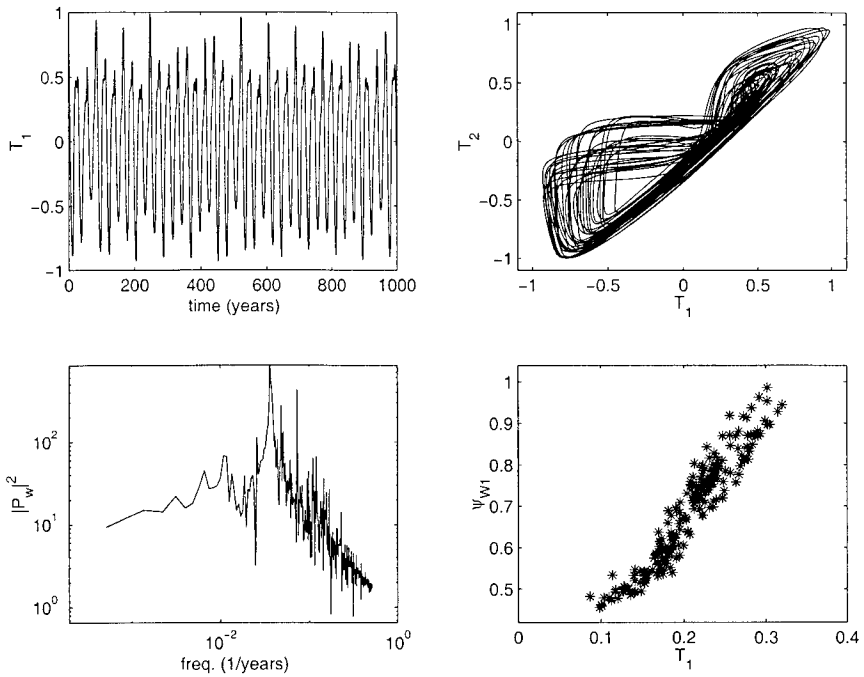

FIG. 7. Analysis of the time series at the latitude $y = 4000$ km corresponding to a solution in the chaos 1 region. (top left) Time series and (bottom left) corresponding power spectrum of the zonally averaged temperature anomaly in the Pacific Ocean, $\overline{T}_1$. (top right) Phase plane of the zonally averaged ocean temperature anomalies $\overline{T}_1$ and $\overline{T}_2$ and (bottom right) associated Poincarè section projected onto the plane of the Pacific zonally averaged temperature $\overline{T}_1$ and the interior transport at the western edge ψ_{W1}.

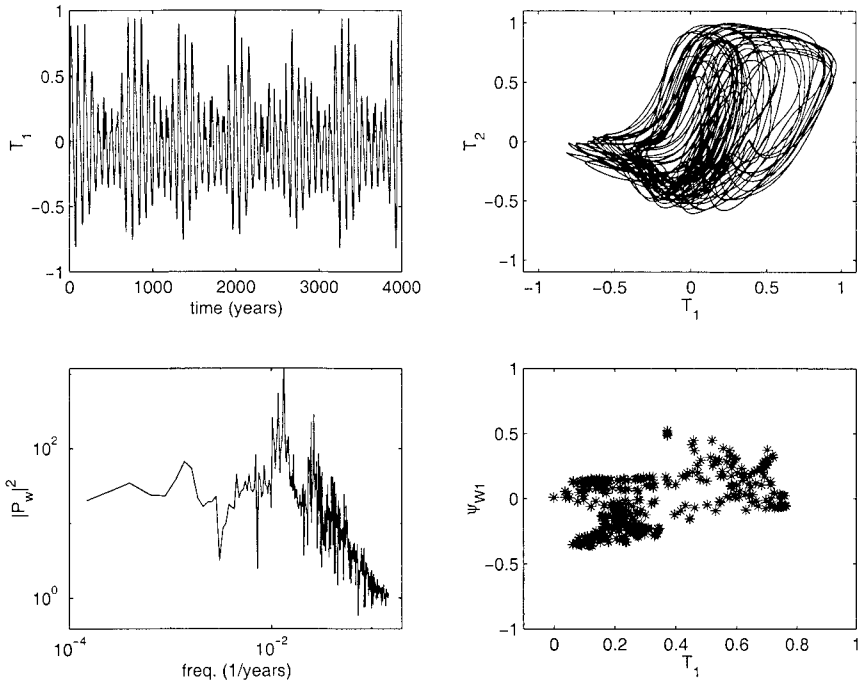

FIG. 8. As in Fig. 7 but for a solution in the chaos 2 region. Notice that the frequency range for the power spectrum is shifted to values lower than those of Fig. 7.

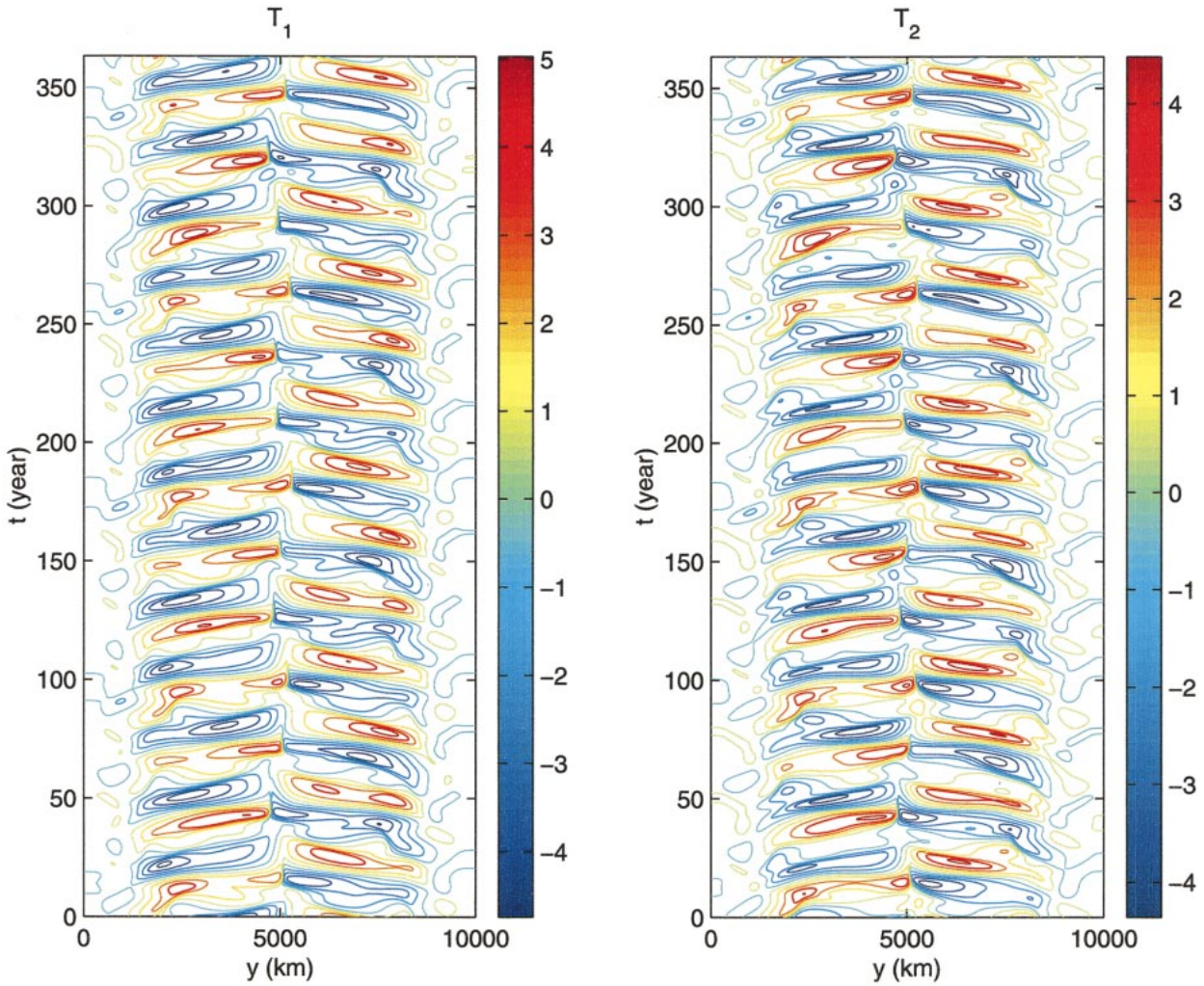

FIG. 9. Anomalies of the zonally averaged temperatures in the (left) Pacific and (right) Atlantic basins as a function of latitude and time, corresponding to the solution in the chaos 1 region. The units in the color bars are degrees Celsius and the peaks of the ocean temperature anomalies $\overline{T}_1$ and $\overline{T}_2$ are 6° and 5.4°C, respectively.

values of $\overline{T}_2$, projected on the plane $\overline{T}_1 - \psi_{W1}$. The anomalies have been normalized by their maximum value. From these figures, it is already possible to observe some qualitative differences between the solutions in the chaos 1 and chaos 2 regions. In particular, the time series of $\overline{T}_1$ in the chaos 2 region has irregular bursts every several hundred years. The bursts are associated with the alternation in the intensity of the anomalies between the subtropical and the subpolar gyres. This alternation is associated with a substantial power at low frequencies of chaos 2 solutions, illustrated by the two broad peaks, centered at 83 and 37 yr, in Fig. 8. In contrast, the chaos 1 solution of Fig. 7 has a single peak centered at decadal timescales (cf. the spectra in Figs. 7 and 8).

In both cases the time series contain the features of a chaotic signal, with dense broadband spectra, convoluted phase portraits, and diffuse Poincarè sections. In order to be certain of the chaotic nature of the attractor and to rule out the possibility of a high-dimensional quasiperiodic structure, we have checked the sensitivity of the solutions to very small perturbations in the initial fields. The exponential divergence of initially neighboring trajectories (not shown here) confirms the existence of chaos in our solutions.

Figures 9 and 10 show the ocean temperature anomalies $\overline{T}_1$ (left panel) and $\overline{T}_2$ (right panel) as a function of latitude and time and corresponding to the same two points in the parameter space as in Figs. 7 and 8, respectively. In both cases, the spatial antisymmetry about the central latitude of the domain that characterizes the anomalies of the periodic solutions is lost. That is, chaos is associated with the excitation of perturbations with a nonsymmetric spatial structure. This symmetry breaking occurs when the small-scale heat diffusion at the intergyre boundary is so weak that the atmospheric heat transport becomes locally very large. This state is unstable to perturbations that allow oceanic mass transport

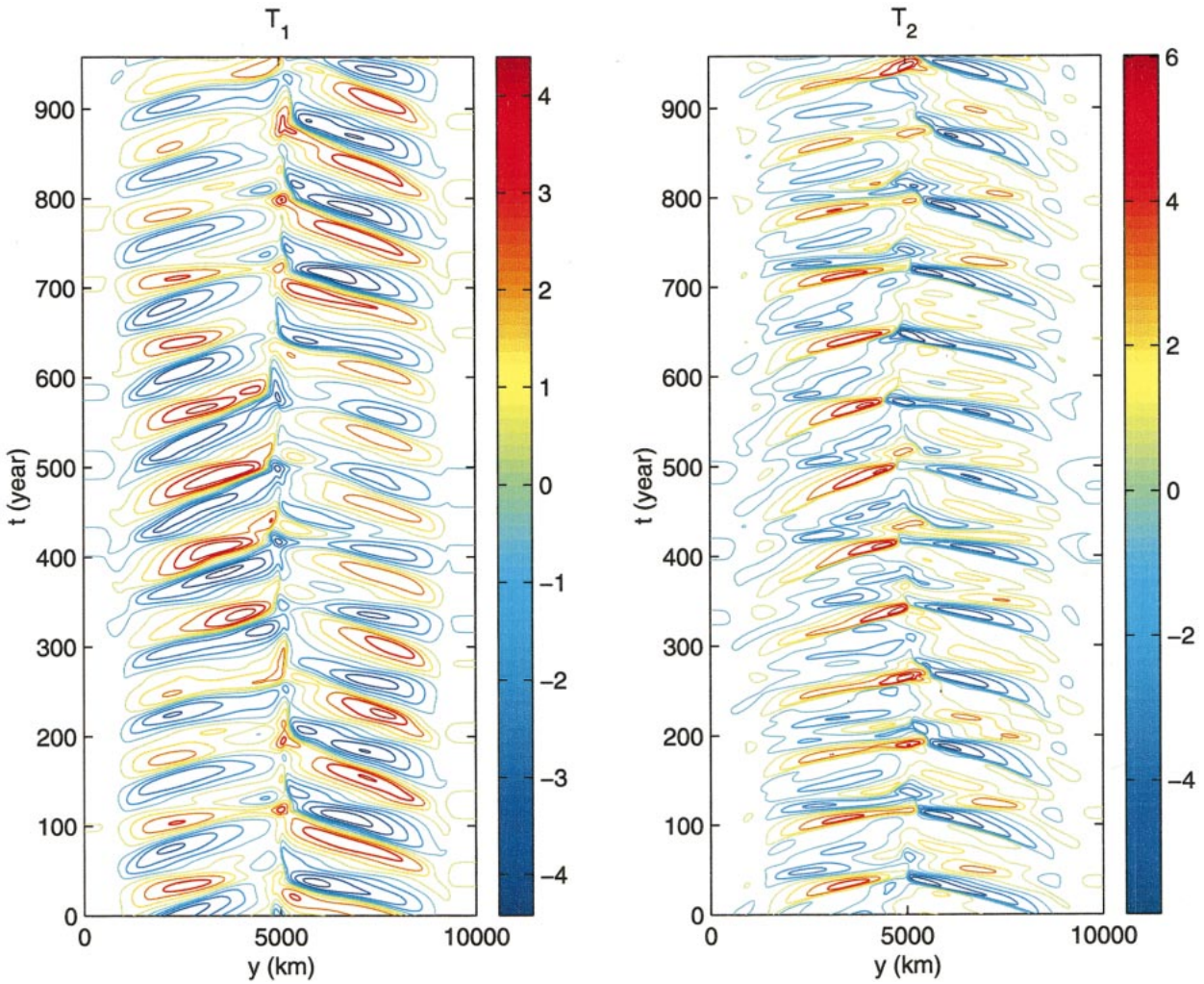

FIG. 10. As in Fig. 9 but for the solution in the chaos 2 region. The peaks of the ocean temperature anomalies $\overline{T}_1$ and $\overline{T}_2$ are 5.4° and 7.3°C, respectively.

across the central latitude of the basin, so that the intergyre exchange of heat is more efficiently achieved by the advective heat transport. This process is associated with a new oscillatory mode with an asymmetric spatial structure and this leads to chaos.

In the chaos 1 regime (Fig. 9), the maximum and minimum amplitudes of the anomalies are approximately of the same size in the subtropical and subpolar gyres at every main cycle. In the chaos 2 regime (Fig. 10), there is a strong asymmetry between the amplitude of the anomalies in the subpolar and subtropical gyres that alternates every several hundred years. This is especially evident in the Pacific basin. For both chaotic regimes, the amplitude of the temperature anomalies in this region of the parameter space is larger than that of the anomalies in the phase-locked regime described in section 3a.

Despite the chaotic nature of the solutions, there is a high degree of correlation between the temperature anomalies in the two basins. Figure 11 shows the correlations between the anomalies of $\overline{T}_1$ and $\overline{T}_2$, for the chaotic solutions shown in Figs. 7 and 9 and in Figs. 8 and 10. The top panel shows the correlation at zero lag for the chaos 1 solution illustrated in Figs. 7 and 9: in the gyres centers, where the anomalies have a substantial amplitude, the correlation of the two chaotic time series is above 0.9. The bottom panel shows the correlations at zero lag (solid line) and the correlation at 9-yr lag (dashed line) for the chaotic solution of Figs. 8 and 10. When the large basin ($\overline{T}_1$) leads the small one ($\overline{T}_2$) by 9 yr, the solutions are most correlated in the gyres' centers. Thus, for this range of parameters, we find high correlation between the two basins, and this is indicative of low-order chaos.

The unrealistic size of the western boundary layer width used in this section does not lead to unrealistic time-averaged mass and heat boundary layer transports. Figure 12 shows various time-averaged fields for the

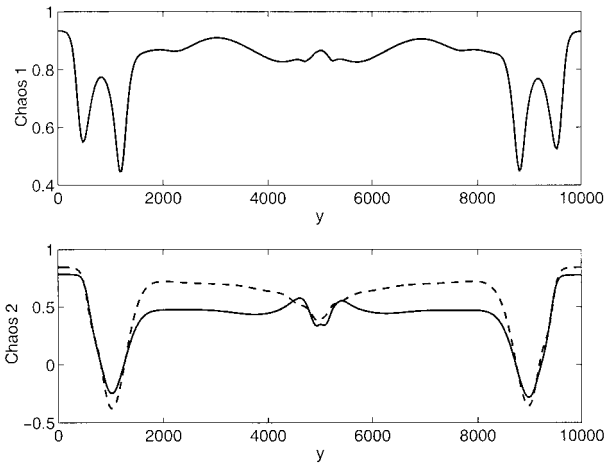

FIG. 11. Pointwise correlations between the anomalies of zonally averaged basin temperatures, $\overline{T}_1$ and $\overline{T}_2$, as a function of latitude in the chaotic regimes. (top) The correlation at zero lag in the chaos 1 regime (all the parameters are as in Figs. 7 and 9). (bottom) The correlation at zero lag (solid line) and the correlation with $\overline{T}_1$ leading $\overline{T}_2$ by 9 yr in the chaos 2 regime (all the parameters are as in Fig. 8 and 10).

chaos 2 solution discussed above (the chaos 1 solution has a similar climatology). A comparison between Fig. 2 and Fig. 12 illustrates that the two sets of mean fields differ by a factor of 2 at most. Specifically, the oceanic heat transports in the chaotic regime are about 2 times those in the phase-locked regime, while the maxima of the interior oceanic mass transports are displaced closer to the center of the basin and are smaller by a factor of 2. Because the symmetry-breaking chaotic motion reduces the average temperature gradient near the intergyre boundary, the averaged wind stress curl is reduced.

4. The regime diagram

In this section we present a low-dimensional cut in the parameter space that captures most of the different regimes exhibited by the model. There are several parameters that control the qualitative behavior of the system:

- the bulk heat transfer coefficient λ, which measures both the rate at which the ocean temperature relaxes toward the temperature of the atmosphere and the amount by which changes in the ocean temperature feedback onto the wind-driven circulation,
- the western boundary layer widths δ_i, which measure the strength of the western boundary currents and can be used to control the importance of the oceanic northward heat transport and thus the delayed feedback between the atmosphere and the ocean, and
- the Rossby deformation radii R_i, which control the long Rossby wave delay times of oceanic adjustment to changes in the atmospheric wind stress for given basin sizes.

Therefore, R_i can be used to control the intrinsic timescale of variability in each basin.

Here, we choose to explore a plane in the parameter

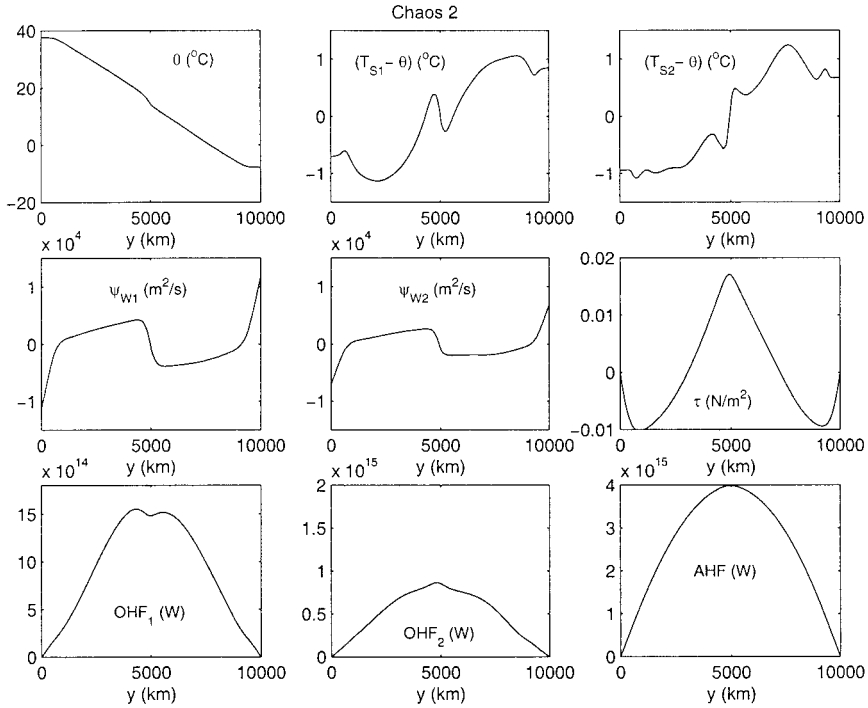

FIG. 12. The time-averaged fields associated with the chaotic solution shown in Fig. 10. The averaged oceanic heat transports peak at 2 times the values shown in Fig. 2, while the oceanic interior transports are one-half those of the phase-locked averages.

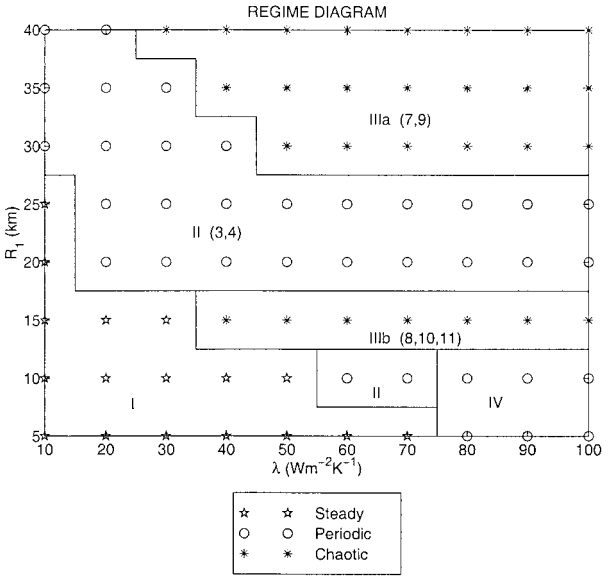

FIG. 13. Two-dimensional cut in the parameter space of the system of (16) and (17). The ordinate corresponds to changes in the parameter R_1. The abscissa corresponds to simultaneous changes in the parameters λ, $\delta_1 = \delta_2$, and ϵ, keeping $\lambda^2\delta_i$ and ϵ/λ constant. This regime diagram contains the three different kind of solutions found in the system: steady, periodic, and chaotic. It has been divided into five regions: oscillation death (region I), phase locking (region II), chaos 1 (region IIIa), chaos 2 (region IIIb), and chaos death (region IV). The figure number of a solution representative of each regime is given in parentheses.

space where one dimension corresponds to changes in R_1 while the other dimension corresponds to simultaneous changes in the parameters ϵ, λ, and $\delta_1 = \delta_2$, with $\lambda^2\delta_i$ and ϵ/λ held constant. Thus when λ is increased δ_i is reduced and ϵ is increased.

For given basin sizes and fixed R_2, varying R_1 changes the difference between the oceanic delay times and therefore alters the frequency offset between the two ocean basins. On the other hand, changing λ varies the strength of the ocean–atmosphere coupling. We decrease δ_i while increasing λ, in order to capture a larger set of behaviors. In particular, from (16) it is clear that ψ_{Wi} is proportional to $\Gamma\lambda T_i$, so that the ratio of the instantaneous feedback [the second term on the right-hand side of (17)] to the delayed feedback [the first term on the right-hand side of (17)] is controlled by the combination $(\Gamma\Upsilon_i)^{-1} \propto \lambda\delta_i/\Gamma$. Because in the range examined presently, Γ^{-1} is dominated by λ, decreasing δ_i while keeping $\lambda^2\delta_i$ constant, increases the nonlinear delayed diffusion at the same rate as the instantaneous coupling.

The different regimes obtained in this parameter plane are shown in Fig. 13. Along the vertical axis, R_1 is varied from 5 to 40 km, corresponding to a range of delay times given by 563 yr $> t_{o1} >$ 8.2 yr. Along the horizontal axis, λ is varied from 10 to 100 W m^{-2} °C^{-1} while varying $\delta_1 = \delta_2$ from 130 to 1.3 km and ϵ from 275 to 2750 m^2 s^{-1}. For the larger values of λ, the δ_i become very small. This is required for the chaotic behavior to appear as commented in section 3c. For these calculations, $R_2 = 30$ km (corresponding to a delay $t_{o2} = 8.7$ yr), $H_1 = H_2 = 1$ km and all other parameters have the values given in Table 1.

The regime diagram presented here contains the three different kinds of solutions of the coupled system: steady, periodic, and chaotic. It has been divided into five regions: oscillation death (region I), phase locking (region II), chaos 1 (region IIIa), chaos 2 (region IIIb), and chaos death (region IV). In this diagram, the uncoupled Atlantic basin has steady solutions for $\lambda < 20$ W m^{-2} °C^{-1} and sustained periodic solutions elsewhere. Meanwhile, the uncoupled Pacific basin has both periodic and chaotic solutions. The latter occurs for large values of λ and in two different regions. One region corresponds to small values of R_1 and occupies the area of chaos death solutions (IV). The other region lies within the area of chaos 1 solutions and corresponds to large values of R_1 (IIIa).

The nature of the solutions has been determined by analyzing the time series resulting from the time integration of the model equations. This analysis includes trajectory plots, phase portraits, Poincarè maps, power spectrum, and sensitivity to initial conditions (cf. Drazin 1992). Detailed bifurcation analysis including the routes to chaos, the structure of the chaotic attractors, and the detection of intermediate quasiperiodic states are not addressed here.

a. Steady solutions: The oscillation death region

In the oscillation death region I, the anomalies of the two basins decay in time and the system eventually reaches a steady state. This behavior appears both when the two uncoupled basins have sustained periodic oscillations and when the oscillations of the uncoupled Atlantic are damped. As explained in section 3b, oscillation death requires the difference between the oceanic delay times to be above a critical value. Here, this critical value corresponds approximately to $\Delta = 0.5$ ($R_1 \approx 28$ km) for $\lambda = 10$ W m^{-2} °C^{-1} and increases as λ becomes larger.

b. Periodic solutions: The phase locking and chaos death regions

The periodic solutions are characterized by thermal anomalies of both basins oscillating periodically in time at a common frequency (or frequencies) and with a constant phase lag. The synchronous temperature anomalies are large scale in space, occupying the full latitudinal span of the gyres and preserve the antisymmetry with respect to the intergyre boundaries imposed by the radiative forcing, as illustrated in Fig. 3. Periodic solutions can arise from two types of coupling-induced processes: the two basins have either damped or sustained oscillations when uncoupled, which then synchronize into a limit cycle (phase locking); at least one of the two basins

is chaotic when uncoupled, but the coupled system is perfectly periodic (chaos death). The region of phase-locked solutions (denoted by the symbol II in Fig. 13) appears for $\lambda = 10$ W m^{-2} °C^{-1}, when $R_1 \geq 28$ km and is confined to intermediate values of R_1 as λ increases. The region of chaos death occurs for large values of λ (this behavior is denoted by the symbol IV in Fig. 13). Analogously to the oscillation death, the appearance of chaos death requires a large enough difference between the ocean delay times.

c. *Chaotic solutions: The chaos 1 and chaos 2 regions*

The chaotic solutions are characterized by anomalies in the two basins fluctuating aperiodically in time. The temperature anomalies break the spatial symmetry with respect to the intergyre boundary that is characteristic of the periodic solutions. The chaotic solutions fall into two categories (chaos 1 and chaos 2). They are described in section 3c. The main difference is that in the chaos 2 regime the system exhibits low-frequency fluctuations that alternate the amplitude of the decadal variability between the subtropical and the subpolar gyres, as illustrated in Fig. 10. The two chaotic behaviors are also conceptually different because in the region of parameter space where chaos 1 arises (denoted by IIIa in Fig. 13), at least one of the basins exhibits chaotic behavior when uncoupled. In contrast, in the region of parameter space where chaos 2 is found (denoted by IIIb in Fig. 13), both uncoupled basins have periodic solutions. Chaos 2 appears for intermediate to large values of λ and for values of R_1 centered around 15 km. Chaos 1 occurs for intermediate to large values of λ and for $R_1 > 30$ km (including the case where $t_{o1} = t_{o2}$), and a typical time–latitude plot of the temperature anomalies in this regime is shown in Fig. 9.

5. Summary and conclusions

The idealized model describing the coupled dynamics of the midlatitude atmosphere and the wind-driven ocean circulation formulated in GC00 has been extended to include two ocean basins. The basins are connected to each other through their coupling to the common zonally averaged atmosphere, which takes place via wind stress and heat fluxes at the air–sea interface.

Our formulation indicates that the most important parameter controlling the interaction between the two ocean basins is the difference between their adjustment times to changes in the wind stress. Three basic kinds of solutions have been found, as follows.

- Phase-locked solutions are those in which the anomalies of the two basins oscillate periodically in time at a common frequency. The oceanic and atmospheric northward heat transports fluctuate approximately in quadrature and there is a phase shift between the oceanic transports in the Atlantic and the Pacific of a few years.
- Oscillation death solutions are those in which the periodic fluctuations decay in time and the system eventually reaches a steady state.
- Chaotic solutions are those in which the anomalies of the two basins fluctuate aperiodically in time with a high degree of correlation. These solutions break the spatial symmetry of the forcing and have broadband spectra with centennial, as well as decadal, variability.

The phase-locked and oscillation death solutions are found within a broad range of values of the model parameters. They include both the case in which the two basins, when uncoupled, have sustained periodic oscillations as well as the case in which the oscillations of the Atlantic are damped, with the latter occurring for more realistic values of the western boundary layer widths. Thus, for the most earthlike range of parameters, our model predicts two kinds of behavior: either the Atlantic Ocean is too small to exhibit sustained oscillations by itself, but can oscillate if driven by the wider Pacific Ocean; or the presence of the Atlantic suppresses the ability of the Pacific basin to exhibit sustained oscillations.

One conclusion suggested by our model is that for coupled modes of variability involving the zonally averaged structure of the atmosphere, the timescales observed *in the Atlantic* are dictated by the transit time of baroclinic Rossby waves *in the Pacific*, which are substantiatially longer than those in the Atlantic. This might explain why several coupled ocean–atmosphere modeling studies (Grotzner et al. 1998; Selten et al. 1999; Zorita and Frankignoul 1997) find the timescales of SST decadal variability in the North Atlantic to be comparable to those in the North Pacific, while the respective baroclinic Rossby waves transit times are quite different.

We also find that the oceanic signal in the Pacific, as represented by the upper-ocean flow in the western boundary current, leads that in the Atlantic by about five years, which is about one-eighth of the common period of the oscillation. Suggestions that the variability in the North Atlantic sector on a timescale of 20 yr is correlated to signals occurring in the North Pacific 2–4 yr earlier is reported in the modeling studies of Zorita and Frankignoul (1997). If the lag in the Atlantic response with respect to the Pacific proves to be a robust feature in the dynamics of coupled atmosphere–oceans system, it could improve the predictability of phenomena associated with shifts in the Atlantic Oceanic temperature.

There are significant differences between the Atlantic and the Pacific that have not been included here. Most notably, there is a thermohaline circulation in the Atlantic, and the tropical El Niño–Southern Oscillation (ENSO) variability influences the North Pacific. Both phenomena have timescales in the decadal range. Other

neglected sources of variability are intrinsic fluctuations within each oceanic basin and those internal to the atmosphere. All the processes uncorrelated between the Atlantic and Pacific sectors can mask any interbasin signal. Long time series are required in order to average out the noise and detect a signature of interbasin organization mediated by the atmosphere.

One possible extension to the present study is to add a stochastic atmospheric component, which must be zonally symmetric within the context of our formulation. We expect that annular white stochastic noise would not alter the delayed feedback mechanism leading to the oscillations. Because the response to noisy forcing is filtered by the associated deterministic system, an oscillatory behavior would still emerge unless the amplitude of the noise were so large as to mask it.

Our simplified model also exhibits chaotic solutions characterized by coupling-induced variability at centennial, as well as decadal timescales. In this regime, the amplitude of the oceanic temperature fluctuations is substantially larger than that observed in nature, but this might be due to some unnecessary simplifications (e.g., the idealized shape of the radiative forcing). It is possible that adding noise to the system would induce chaotic behavior within a more realistic range of parameters, thus leading to a more realistic amplitude of the anomalies.

Acknowledgments. Two anonymous referees are thanked for their constructive criticism. Funding for this research is provided by the Department of Energy and the National Science Foundation.

REFERENCES

Anderson, D., and A. Gill, 1975: Spin-up of a stratified ocean, with applications to upwelling. *Deep-Sea Res.,* **22,** 583–596.

Barnett, T., D. Pierce, R. Saravanan, N. Schneider, D. Dommenget, and M. Latif, 1999: Origins of the midlatitude Pacific decadal variability. *Geophys. Res. Lett.,* **26,** 1453–1456.

Battisti, D. S., U. S. Bhatt, and M. A. Alexander, 1995: A modeling study of the interannual variability in the wintertime North Atlantic Ocean. *J. Climate,* **8,** 3067–3083.

Berloff, P., and S. Meacham, 1997: The dynamics of an equivalent-barotropic model of the wind-driven circulation. *J. Mar. Res.,* **55,** 407–451.

Bjerknes, J., 1964: Atlantic air–sea interaction. *Advances in Geophysics,* Vol. 10, Academic Press, 1–82.

Bladè, I., 1997: The influence of midlatitude ocean–atmosphere coupling on the low-frequency variability of a GCM. Part I: No tropical SST forcing. *J. Climate,* **10,** 2087–2106.

Budyko, M., 1969: The effect of solar radiation variations on the climate of the earth. *Tellus,* **21,** 611–619.

Cessi, P., 2000: Thermal feedback on wind-stress as a contributing cause of climate variability. *J. Climate,* **13,** 232–244.

Chelton, D. B., R. A. deSzoeke, M. G. Schlax, K. El Naggar, and N. Siwertz, 1998: Geographical variability of the first baroclinic Rossby radius of deformation. *J. Phys. Oceanogr.,* **28,** 433–460.

Chen, F., and M. Ghil, 1995: Interdecadal variability of the thermohaline circulation and high latitude surface fluxes. *J. Phys. Oceanogr.,* **25,** 2547–2568.

Curry, R., M. McCartney, and T. Joyce, 1998: Oceanic transport of subpolar climate signals to mid-depth subtropical waters. *Nature,* **391,** 575–577.

Delworth, T., 1996: North Atlantic interannual variability in a coupled ocean–atmosphere model. *J. Climate,* **9,** 2356–2375.

——, S. Manabe, and R. Stouffer, 1993: Interdecadal variations of the thermohaline circulation in a coupled ocean–atmosphere model. *J. Climate,* **6,** 1993–2011.

Deser, C., and M. Blackmon, 1993: Surface climate variations over the North Atlantic Ocean during winter: 1900–1989. *J. Climate,* **6,** 1743–1753.

——, M. Alexander, and M. Timlin, 1996: Upper-ocean thermal variations in the North Pacific during 1970–1991. *J. Climate,* **9,** 1840–1855.

Drazin, P., 1992: *Nonlinear Systems.* Cambridge University Press, 317 pp.

Frankignoul, C., P. Muller, and E. Zorita, 1997: A simple model of the decadal response of the ocean to stochastic wind forcing. *J. Phys. Oceanogr.,* **27,** 1533–1546.

Gallego, B., and P. Cessi, 2000: Exchange of heat and momentum between the atmosphere and the ocean: A minimal model of decadal oscillations. *Climate Dyn.,* **16,** 479–489.

Goodman, J., and J. Marshall, 1999: A model of decadal middle-latitude atmosphere–ocean coupled modes. *J. Climate,* **12,** 621–641.

Graham, N., 1994: Decadal-scale climate variability in the tropical and North Pacific during the 1970s and 1980s. Observations and model results. *Climate Dyn.,* **10,** 135–162.

Green, J., 1970: Transfer properties of the large scale eddies and the general circulation of the atmosphere. *Quart. J. Roy. Meteor. Soc.,* **96,** 157–185.

Griffies, S., and E. Tziperman, 1995: A linear thermohaline oscillator driven by stochastic atmospheric forcing. *J. Climate,* **8,** 2440–2453.

Grötzner, A., M. Latif, and T. P. Barnett, 1998: A decadal climate cycle in the North Atlantic Ocean as simulated by the ECHO coupled GCM. *J. Climate,* **11,** 831–847.

Haney, R., 1971: Surface thermal boundary condition for ocean circulation models. *J. Phys. Oceanogr.,* **1,** 241–248.

Hurrel, J., 1995: Decadal trends in the North Atlantic oscillation regional temperatures and precipitation. *Science,* **269,** 676–679.

Jin, F., 1997: A theory of interdecadal climate variability of the North Pacific ocean–atmosphere system. *J. Climate,* **10,** 1821–1835.

Kushnir, Y., 1994: Interdecadal variations in North Atlantic sea surface temperature and associated atmospheric conditions. *J. Climate,* **7,** 141–157.

——, and J. M. Wallace, 1989: Low-frequency variability in the Northern Hemisphere winter: Geographical distribution, structure and time-scale dependence. *J. Atmos. Sci.,* **46,** 3122–3142.

Latif, M., and T. Barnett, 1994: Causes of decadal climate variability over the North Pacific and North America. *Science,* **266,** 634–637.

——, and T. Barnett, 1996: Decadal climate variability over the North Pacific and North America: Dynamics and predictability. *J. Climate,* **9,** 2407–2423.

——, K. Arpe, and E. Roeckner, 2000: Oceanic control of decadal North Atlantic sea level pressure variability in winter. *Geophys. Res. Lett.,* **27,** 727–730.

Levitus, S., J. Antonov, and T. Boyer, 1994: Interannual variability of temperature at a depth of 125 meters in the North Atlantic ocean. *Science,* **266,** 96–99.

Lorenz, E., 1967: *The Nature and Theory of the General Circulation of the Atmosphere.* World Meteorological Organization, 161 pp.

McCartney, M., R. Curry, and H. Bezdec, 1997: North Atlantic's transformation pathway. *Oceanus,* **39,** 19–23.

Meehl, G., J. M. Arblaster, and W. G. Strand Jr., 1998: Global scale decadal climate variability. *Geophys. Res. Lett.,* **25,** 3983–3986.

Moses, T., G. Kiladis, H. Diaz, and R. Barry, 1987: Characteristics and frequency reversals in mean sea level pressure in the North Atlantic sector and their relationships in long-term temperature trends. *J. Climatol.,* **7,** 13–30.

Munich, M., M. Latif, S. Venzke, and E. Maier-Reimer, 1998: Decadal oscillations in a simple coupled model. *J. Climate,* **11,** 3309–3319.

Nakamura, H., G. Lin, and T. Yamagata, 1997: Decadal climate variability in the North Pacific during recent decades. *Bull. Amer. Meteor. Soc.,* **78,** 2215–2225.

Namias, J., 1959: Recent seasonal interactions between North Pacific waters and the overlying atmospheric circulation. *J. Geophys. Res.,* **64,** 631–646.

——, 1963: Large-scale air–sea interactions over the North Pacific from summer (1962) through the subsequent winter. *J. Geophys. Res.,* **68,** 6171–6186.

Parker, T., and C. Folland, 1988: The nature of climatic variability. *Meteor. Mag.,* **117,** 201–210.

Pavan, V., and I. Held, 1996: The diffusive approximation for eddy fluxes in baroclinically unstable jets. *J. Atmos. Sci.,* **53,** 1262–1272.

Salmon, R., 1998: *Lectures on Geophysical Fluid Dynamics.* Oxford University Press, 378 pp.

Saravanan, R., 1998: Atmospheric low-frequency variability and its relationship to midlatitude SST variability: Studies using the NCAR Climate System Model. *J. Climate,* **11,** 1386–1404.

——, and J. McWilliams, 1997: Stochasticity and spatial resonance in interdecadal climate fluctuations. *J. Climate,* **10,** 2299–2320.

——, G. Danabasoglu, S. Doney, and J. McWilliams, 2000: Decadal variability and predictability in the midlatitude ocean–atmosphere system. *J. Climate,* **13,** 1073–1097.

Selten, F., R. Haarsma, and J. Opsteegh, 1999: On the mechanism of North Atlantic decadal variability. *J. Climate,* **12,** 1956–1973.

Spall, M., 1996: Dynamics of the Gulf Stream/deep western boundary current crossover. Part II: Low-frequency internal oscillations. *J. Phys. Oceanogr.,* **26,** 2169–2182.

Speich, S., H. Dijkstra, and M. Ghil, 1995: Succesive bifurcations in a shallow-water model applied to the wind-driven ocean circulation. *Nonlinear Processes Geophys.,* **2,** 241–268.

Sun, D.-Z., and R. S. Lindzen, 1994: A PV view of the zonal mean distribution of temperature and wind in the extratropical troposphere. *J. Atmos. Sci.,* **51,** 757–772.

Thompson, D. W. J., and J. M. Wallace, 2000: Annular modes in the extratropical circulation. Part I: Month-to-month variability. *J. Climate,* **13,** 1000–1016.

Timmermann, A., M. Latif, R. Voss, and A. Grotzner, 1998: Northern Hemispheric interdecadal variability: A coupled air–sea mode. *J. Climate,* **11,** 1906–1931.

Trenberth, K., and J. Hurrell, 1994: Decadal atmosphere–ocean variations in the Pacific. *Climate Dyn.,* **9,** 303–319.

Venzke, S., M. R. Allen, R. T. Sutton, and D. P. Rowell, 1999: The atmospheric response over the North Atlantic to decadal changes in sea surface temperature. *J. Climate,* **12,** 2562–2584.

Wallace, J., and D. Gutzler, 1981: Teleconnections in the geopotential height field during the Northern Hemisphere winter. *Mon. Wea. Rev.,* **109,** 784–812.

Wang, X., P. Stone, and H. Marotzke, 1995: Poleward heat transport in a barotropic ocean model. *J. Phys. Oceanogr.,* **25,** 256–265.

Weaver, A., and E. Sarachik, 1991: Evidence for decadal variability in an open general circulation model—an advective mechanism. *Atmos.–Ocean,* **29,** 197–231.

——, ——, and J. Marotzke, 1991: Freshwater flux forcing of decadal and interdecadal oceanic variability. *Nature,* **353,** 836–838.

Weng, W., and J. D. Neelin, 1999: Analytical prototypes for ocean–atmosphere interaction at midlatitudes. Part II: Mechanisms for coupled gyre modes. *J. Climate,* **12,** 2757–2774.

White, W., and D. Cayan, 1998: Quasi-periodic and global symmetries in interdecadal upper ocean temperature variability. *J. Geophys. Res.,* **103,** 21 335–21 354.

Winton, M., and E. Sarachik, 1993: Thermohaline oscillations induced by strong steady salinity forcing of ocean general circulation models. *J. Phys. Oceanogr.,* **23,** 1389–1410.

Zhang, R., and S. Levitus, 1997: Structure and clycle of decadal variability of upper-ocean temperature in the North Pacific. *J. Climate,* **10,** 710–727.

Zorita, E., and C. Frankignoul, 1997: Modes of North Atlantic decadal variability in the ECHAM1/LSG coupled ocean–atmosphere general circulation model. *J. Climate,* **10,** 183–200.